

Cite this: *Nanoscale Adv.*, 2019, 1, 4895

# Lightweight, mechanically flexible and thermally superinsulating rGO/polyimide nanocomposite foam with an anisotropic microstructure†

Yuyang Qin,<sup>‡</sup> Qingyu Peng,<sup>‡</sup> Yue Zhu,<sup>a</sup> Xu Zhao,<sup>a</sup> Zaishan Lin,<sup>a</sup> Xiaodong He<sup>ac</sup> and Yibin Li<sup>\*ac</sup>

We report that lightweight, anisotropic, mechanically flexible, and high performance thermally insulating materials are fabricated by the assembly of graphene oxide (GO) and polyimide (PI). With an appropriate ratio between GO and PI building blocks, the rGO/PI thermally insulating material exhibits hierarchically aligned microstructures with high porosity. These microstructures endow the rGO/PI nanocomposite with low mass density and super-insulating property (extremely low thermal conductivity of  $0.012 \text{ W m}^{-1} \text{ K}^{-1}$  in the radial direction). Meanwhile, the introduction of PI enhances the mechanical strength and thermal stability of rGO foam. Our rGO/PI nanocomposites as super-insulating foams with a low thermal conductivity are highly attractive for potential thermal insulation applications in aerospace, wearable devices, and energy-efficient buildings.

Received 17th July 2019  
Accepted 27th October 2019

DOI: 10.1039/c9na00444k

rsc.li/nanoscale-advances

## Introduction

With the ever-increasing awareness concerning the global energy crisis and continuous reduction of carbon footprint,<sup>1,2</sup> tremendous interest has been drawn to high-performance thermal insulation materials, particularly in emerging areas such as personal energy management,<sup>3,4</sup> building insulation<sup>5</sup> and space applications. Super-thermal insulation materials have a complex combination of characteristics, including low thermal conductivity, good mechanical flexibility and low mass density.<sup>2,6,7</sup> However, a plateau has been reached in the development of traditional thermal insulation materials. To further enhance thermal insulation properties, undesirable compromises have been made in mechanical flexibility, manufacturing complexity, and performance stability.<sup>8–10</sup> Common fossil-fuel-derived thermally insulating foams, including polyurethane ( $\lambda = 0.02\text{--}0.03 \text{ W m}^{-1} \text{ K}^{-1}$ ), expanded polystyrene foam ( $\lambda = 0.03\text{--}0.04 \text{ W m}^{-1} \text{ K}^{-1}$ ), and porous aramids ( $\lambda = 0.028 \text{ W m}^{-1} \text{ K}^{-1}$ ), are unsatisfactory due to the high thermal conductivities.<sup>6,11–13</sup> Sustainable insulation materials, including wool, natural wood cork and other renewable lignocellulosic biomass, possess high

thermal conductivities close to that of air ( $0.03 \text{ W m}^{-1} \text{ K}^{-1}$ ).<sup>6,14,15</sup> Silicon aerogels have been reported to have a low  $\lambda$  (approximately  $0.02 \text{ W m}^{-1} \text{ K}^{-1}$ ), but the mechanical brittleness makes them susceptible to insulation failure.<sup>16</sup>

Moreover, the typically isotropic microstructure of traditional thermally insulating materials was not ideal for high performance thermal insulation. Rational design of the anisotropic microstructure can lead to even more enhanced functionalities, especially for the thermal insulation and mechanical flexibility properties. For instance, nanowood with naturally aligned nanocellulose shows anisotropic thermal properties ( $0.03 \text{ W m}^{-1} \text{ K}^{-1}$  in the transverse direction and  $0.06 \text{ W m}^{-1} \text{ K}^{-1}$  in the axial direction).<sup>17</sup> The alignment of the anisotropic graphene oxide/nanocellulose nanocomposite can result in an extremely low thermal conductivity of  $0.015 \text{ W m}^{-1} \text{ K}^{-1}$  in the radial direction.<sup>18</sup> Examples of multilayer materials and nanomaterials with unique hierarchical microstructures exhibit significant advances for effective thermal management.<sup>19–23</sup> The anisotropic microstructures could enhance efficient thermal dissipation in the axial direction, thereby effectively preventing heat localization and reducing heat flow across the aligned channels in the radial direction.<sup>17</sup> It would be beneficial for the further improvement of thermal insulation, which cannot be achieved by isotropic thermally insulating materials.

In addition, composite materials with anisotropic microstructures could often achieve enhanced functionalities beyond their instinct performance for the utilization of the advantages of individual components.<sup>24</sup> Current nanosized one- and two-dimensional (1D and 2D) building blocks, such as nanotubes and graphene nanosheets, were widely used in thermally insulating composites for the substantial reduction of solid heat

<sup>a</sup>Center for Composite Materials and Structures, Harbin Institute of Technology, Harbin 150080, P. R. China. E-mail: pengqingyu@hit.edu.cn; liyibin@hit.edu.cn

<sup>b</sup>School of Chemistry and Materials Engineering, Changshu Institute of Technology, Changshu 215500, P. R. China

<sup>c</sup>Shenzhen STRONG Advanced Materials Institute Ltd Corp, Shenzhen 518000, P. R. China

† Electronic supplementary information (ESI) available. See DOI: 10.1039/c9na00444k

‡ These authors contributed equally to this work.



conduction by the effect of phonon barriers.<sup>25,26</sup> Porous structures endow the thermally insulating nanocomposite with low density and thus small solid conductivity, as well as partial suppression of gaseous thermal conductivity.<sup>27</sup> Thus, the formation of hierarchical microstructures and the typical properties of nanosized materials should be given high-priority consideration in the design of more efficient insulating composites.

Here, we present a facile methodology to create a lightweight, highly ordered, and thermally insulating graphene-based nanocomposite with the aid of water-soluble polyimide (PI).<sup>28</sup> rGO/PI insulating materials are achieved by applying freeze-casting and subsequent thermal annealing procedures. Owing to the superior flexible attribute and excellent thermal stability,<sup>29,30</sup> water-soluble PI is incorporated as a reinforcement to improve the mechanical flexibility property and thermal insulation performance of the reduced graphene oxide (rGO) aerogels. The strong orientation effect during the freezing process leads to a hierarchical cellular architecture,<sup>31,32</sup> which endows the nanocomposite with unique anisotropic thermal and mechanical properties.<sup>18</sup> Furthermore, the highly ordered cellular walls of the thermally insulating nanocomposite can effectively impede the heat transport in the radial direction and result in ultra-low in-plane thermal conductivity.<sup>17,33</sup> The exceptional attributes of GO nanosheets and PI polymeric building blocks, along with the intriguing anisotropic architectures, make the as-prepared rGO/PI nanocomposite foams as an attractive option for thermal management.

## Results and discussion

The steps in the synthesis process of rGO/PI thermally insulating nanocomposite are vividly sketched in Fig. 1. To obtain the unique hierarchical architecture, a versatile, optimized, facile and well-controlled unidirectional freezing method, namely freeze casting,<sup>34</sup> was performed to prepare a highly

anisotropic graphene-based scaffold with a homogeneous mixture of a water-soluble PI precursor and GO suspension. During this unique procedure, GO nanosheets and polymeric building blocks were rejected from the growing ice and simultaneously induced to build sophisticated and highly ordered architectures, mimicking the manner of honeycomb-like structures. Afterwards, the resulting monolith was treated by freeze drying, followed by an annealing treatment in an inert gas. Through the process of cryodesiccation, the ice was sublimated, leaving the desired anisotropic scaffold with a negative replica of the ice. With the subsequent annealing procedure, GO nanosheets were partially reduced and water-soluble PI precursors were imidized to PI.<sup>28,35</sup> Due to the readily accessible synthesis procedure, rGO/PI thermally insulating nanocomposites with desired fractions of GO (GO: 10 wt%–30 wt%) were facilely fabricated. With the increasing content of GO, the density of the rGO/PI insulating monolith shows a downtrend (Fig. S1d†). Furthermore, the local volume of the rGO/PI nanocomposite with a high content of PI reveals pronounced shrinkage for substantial relative material loss during the imidization procedure (Fig. S1a and b†). Simultaneously, the relative cellular walls of the nanocomposite were crumpled on account of the uneven stress distribution of the cell walls, yielding a slightly waved scaffold with some ripples and wrinkles (Fig. S1c†), which was similar to PI foam (Fig. S5d†).<sup>36</sup> Moreover, control tests involving rGO/PI thermally insulating nanocomposites with different proportions of GO were conducted to further investigate the mechanical and thermal insulation properties.

The microstructure and morphology of the rGO/PI nanocomposite with the desired content of GO were systematically investigated by a combination of scanning electron microscopy (SEM) and transmission electron microscopy (TEM). Microstructural analysis of the graphene-based nanocomposites reveals significant anisotropic architectures, leading to unique structural and functional capabilities. These highly anisotropic

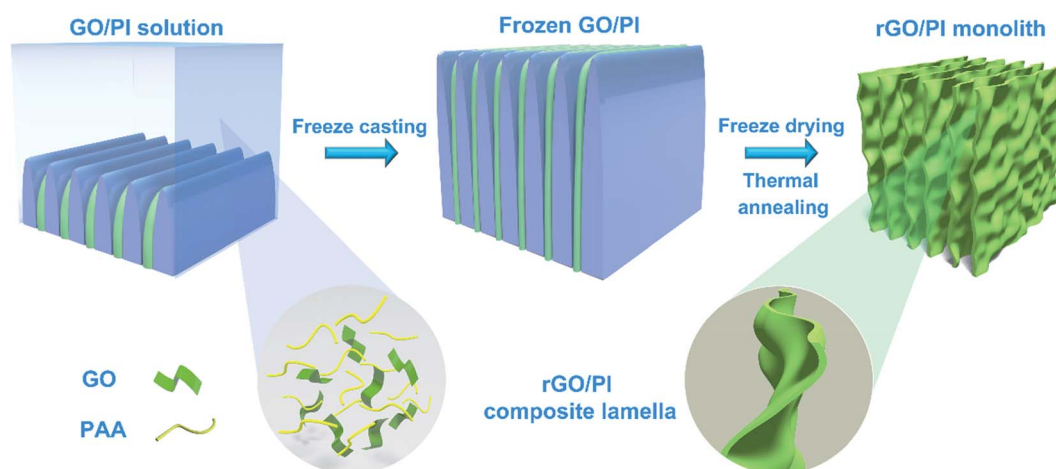


Fig. 1 Structural design of the anisotropic rGO/PI thermally insulating nanocomposite foam with highly ordered structures. Schematic illustration of the fabrication process of the nanocomposite foam by freeze-casting and thermal annealing. The aqueous suspension of GO and water-soluble PI precursor was subjected to directional freezing in a liquid nitrogen bath, followed by thermal annealing to obtain the rGO/PI nanocomposite.



structures can be vividly defined as scaffolds in the axial and radial orientations, which are along and perpendicular to the growth direction of ice respectively (Fig. 2).

As shown in Fig. 2a, a typical top view of the rGO/PI nanocomposite foam with lower content of GO (10 wt%) shows a randomly oriented porous scaffold in the axial direction, which is similar to the disordered three dimensional (3D) graphene-based monolith obtained by common freezing.<sup>37</sup> A magnified SEM image exhibits some curled and twisted fibrils bridging between the adjacent nanocomposite layers. This can be attributed to the great loss of small molecule materials during the thermal annealing process, leading to the structural failure of highly ordered morphology and the pronounced volume shrinkage of the nanocomposite. With the increasing content of GO, the cross-section of the thermally insulating nanocomposite (GO, 20 wt%) gradually reveals continuous and uniform architecture. Compared with the wrinkle-like porous scaffold (Fig. 2a), a smoother cell wall structure can be observed with fewer curled fibrils, as depicted in the magnified SEM image in Fig. 2b. With further increase of the GO content (up to

30 wt%), a honeycomb-like microstructure with aligned tubular pores can be observed (Fig. 2c). The dimensions of the porous architecture show a diameter in the scale of 10–30 micrometers and a cell wall thickness in the range of 0.1–0.3  $\mu\text{m}$ .

Due to the dramatic imidization of the polyimide precursor and thermal reduction of GO, the radially aligned pore structure is transformed into distorted and shrunken architecture, which is not lamellar. It was discovered that the longitudinal section of the nanocomposite monolith (GO, 10 wt%) exhibits highly thick and corrugated micro-channeled scaffolds oriented in random with a great deal of threadlike structures on the edge of the cell walls (Fig. 2d). With the increase of GO content (20 wt%), the rGO/PI nanocomposite exhibits a relatively aligned lamellar microstructure, decreasing the adverse effect of volume shrinkage (Fig. 2e). For a typical rGO/PI nanocomposite with 30 wt% content of GO, a side view of the monolith reveals a vertically aligned microstructure along radial directions, which is ordered in an almost parallel manner (Fig. 2f). Upon magnifying the highly ordered lamellar microstructure, it can be clearly seen that the channel size is estimated to be 20–30

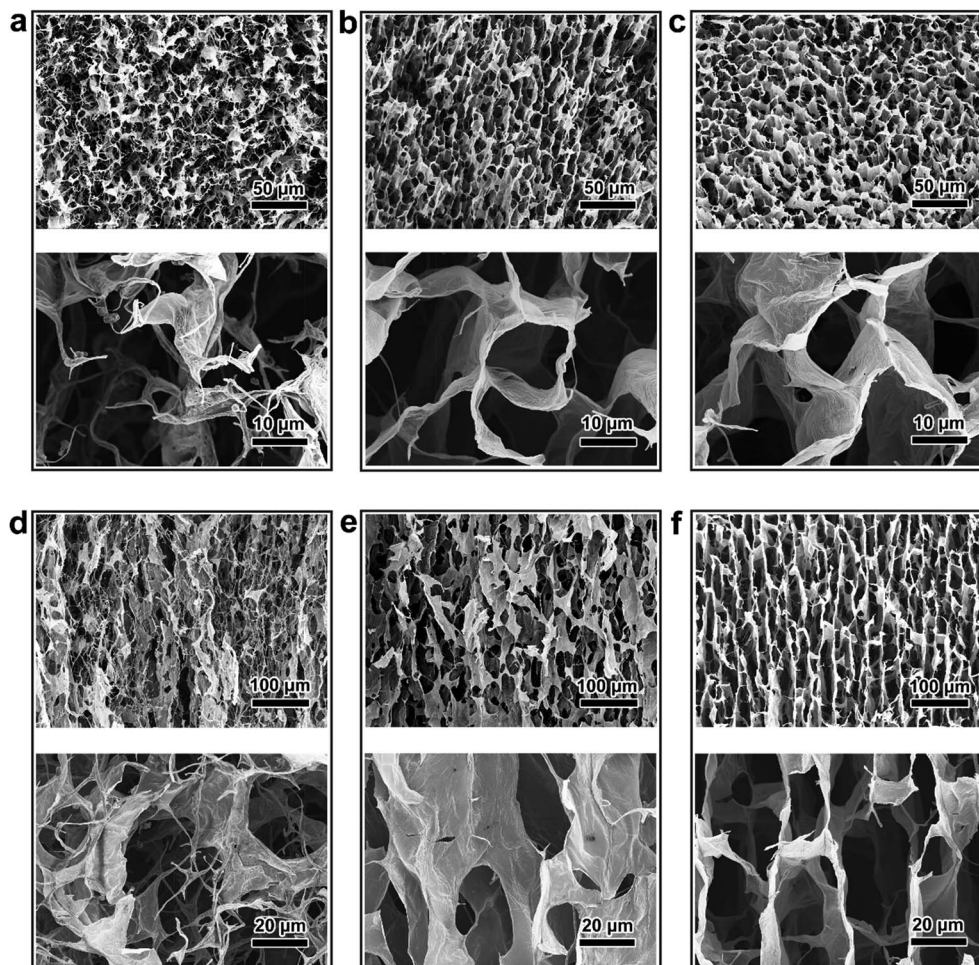


**Fig. 2** Structural characterization of thermally insulating nanocomposite foams with different proportions of GO. (a–c) SEM images of the nanocomposite sample (content of GO from 10 wt% to 30 wt%) perpendicular to the growth direction of ice, revealing the porous scaffold in radial orientation. (d–f) SEM images of the nanocomposite foam (content of GO from 10 wt% to 30 wt%) in the axial direction, clearly showing the cross-section view of the micro-channels along the direction of the ice front. The microstructure of the nanocomposite gradually reveals a highly ordered fashion with increasing content of GO.





um, which is in agreement with the honeycomb-like pore dimension. Moreover, twisted and curled sheets can be observed bridging the adjoining rGO/PI layers, which can be attributed to the uneven stresses produced in the process of lyophilization.<sup>38</sup> On account of the freeze casting mechanism, ice crystals present strong anisotropic growth kinetics along the temperature gradient, resulting in the formation of highly ordered anisotropic porous architectures. This hierarchical microstructure can effectively impede thermal transport and reduce thermal conductivity.

The microstructures of the nanocomposite with different contents of GO are further characterized by TEM. It is noteworthy that carpet-like pristine rGO nanosheets display a two-dimensional morphology with some ripples and wrinkles, as shown in Fig. S2d.† After the introduction of water-soluble PI, rGO nanosheets reveal an encapsulating morphology (Fig. S2a–c†). Compared with the original rGO foam, the freeze-dried rGO/PI nanocomposite exhibits a thicker and nanoscale roughness cell wall structure with some visible dark spots (Fig. S2a†). With the increasing content of GO, the rGO/PI

nanosheets gradually show a relatively flat morphology with some ripples and wrinkles (Fig. S2b and c†).

To investigate the chemical composition and possible bonding interactions between rGO nanosheets and PI building blocks in the thermally insulating nanocomposite, spectroscopic analyses such as Fourier transform infrared (FT-IR) and X-ray photoelectron spectroscopy (XPS) were conducted. After thermal treatment, the FT-IR spectra of rGO exhibit three typical peaks (Fig. 3a), which are ascribed to the broad O–H stretching vibration ( $3435\text{ cm}^{-1}$ ), aromatic C=C stretching vibrations (approximately  $1621\text{ cm}^{-1}$ ) and C–O–C stretching vibrations (about  $1110\text{ cm}^{-1}$ ). Moreover, it can be clearly observed that the characteristic oxidation peaks of GO decrease sharply, indicating the partial reduction of GO.<sup>35</sup> Compared with the normal rGO foam, the characteristic absorption peaks of the rGO/PI nanocomposite can be observed at  $1360\text{ cm}^{-1}$ ,  $1483\text{ cm}^{-1}$ , and  $1706\text{ cm}^{-1}$ , which are assigned to C–N stretching vibration, C=C stretching vibration, and imide C=O symmetric and asymmetric stretches, respectively. It has been clearly documented in the literature that hydrogen bonds and interfacial

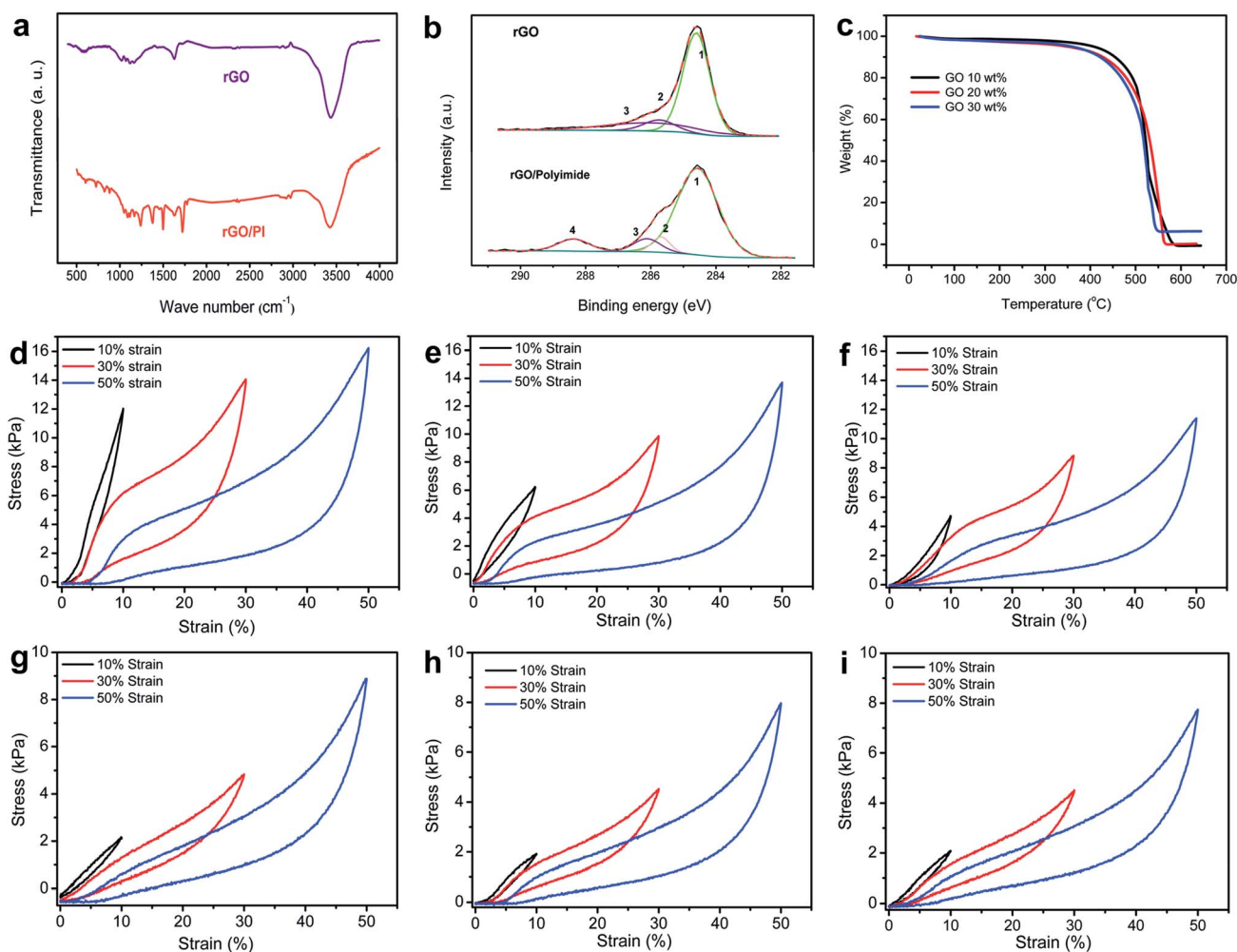


Fig. 3 Chemical structure and mechanical properties of the thermally insulating foam with different contents of GO: (a–c) FT-IR, XPS, and TGA dates for the rGO/PI nanocomposite. (d–f) The stress–strain ( $\sigma$ – $\epsilon$ ) curves of the rGO/PI thermally insulating nanocomposite (GO, 10–30 wt%) with different set strains in the axial direction and (g–i) for the radial direction.



effect contribute to the interaction force between GO and water-soluble PI.<sup>39</sup> The nanoscale surface roughness and high surface area of rGO nanosheets enhance this interaction. The chemical composition of the graphene-based nanocomposite was further investigated by XPS analysis. The C 1s spectra of GO exhibit three peaks at 284.6, 286.6, and 287.8 eV and 288.2 eV, indicating the existence of sp<sup>2</sup> and sp<sup>3</sup> C, C–O single bond, C=O and O–C=O of carboxyl groups, respectively (Fig. S3a†). After thermal annealing, the peak intensity related to C–C (284.6 eV) rises sharply, but the intensities of the peaks of oxidation groups (C–O, C=O, O–C=O) decrease significantly, indicating a high level of reduction (Fig. 3b).<sup>40</sup> With the employment of water-soluble PI, the wide-scan XPS survey spectroscopy of the rGO/PI nanocomposite shows significant peaks located at 284.6 eV (C 1s), 400 eV (N 1s), and 532 eV (O 1s), as shown in Fig. S3b.† Moreover, the C 1s spectrum exhibits four characteristic peaks at 284.6, 285.5, 286.3, and 288.6 eV, corresponding to C=C/C–C, C–N, C–O, and C=O, respectively (Fig. 3b). The thermal stabilities of the graphene-based nanocomposites were measured by thermogravimetric analysis (TGA) (Fig. 3c). With the employment of water-soluble PI, the decomposition temperatures of the rGO/PI monolith with high content of GO are observed at around 462 °C and this decomposition process continues until 540 °C. The increasing content of PI endows the rGO/PI foam with an enhancement of thermal stability (from 462 to 475 °C), which substantially influences the thermal insulation property of this graphene-based nanocomposite. Also, the TGA dates of rGO, PI and rGO/PI nanocomposite were compared to show that the employment of PI could enhance the thermal stability of rGO foam (Fig. S5c†).

To better assess the relationship between the hierarchical microstructure and mechanical properties of the rGO/PI nanocomposite, a set of compressive tests were conducted in axial and radial directions (Fig. 3d–i). The stress–strain curves of rGO/PI aerogels with different contents of GO reveal that the variation of the microstructure plays a vital role in determining the mechanical properties of the nanocomposites.

During the loading process in the axial direction (Fig. 3d), three characteristic regions can be observed in the stress–strain curves, which show the typical deformation behavior of open-cell or honeycomb-like elastomeric foams:<sup>41</sup> the initial linear elastic region at low strain ( $\epsilon < 8\%$ ), corresponding to the elastic cell edge bending; a flat stress plateau region ( $8\% < \epsilon < 35\%$ ), indicative of elastic buckling of the honeycomb-like cell walls; and the steeply increasing stress region ( $\epsilon > 35\%$ ), attributed to densification of the cell walls. As for the loading process in the radial direction (Fig. 3g), however, the curves obtained display two distinct deformation stages, a linear-elastic region at low strain, followed by a densification region with stress rising steeply. This hysteresis loop can be observed in common freezing graphene foam and foam-like carbon nanotube (CNT) films.<sup>37,42</sup> Based on the strain–stress curves of the nanocomposite with different contents of GO, the compressive strength of the nanocomposite in the axial direction is significantly higher than that in the radial structural deformation, analogous to the typical feature of anisotropic cellular foam.<sup>43</sup> This is due to the hierarchical architecture obtained by the

unidirectional freeze-casting mechanism, which endows the nanocomposite with anisotropic mechanical properties. With the increasing content of PI, the maximum stress of rGO/PI nanocomposites (at the same strain) exhibits different growth trends in the axial and radial direction. High content PI could significantly enhance the maximum stress of the nanocomposite in the axial direction (from 11.5 to 15.7 kPa, at a strain of 50%), while a slight increase of the stress in radial orientation (from 7.9 to 9.2 kPa, at strain of 50%). It demonstrates clearly that the employment of PI can effectively improve the mechanical strength of the rGO/PI nanocomposite. Considering the pronounced shrinkage of PI building blocks under the action of significant relative material loss during the imidization procedure, the anisotropic insulating property of the rGO/PI nanocomposite would be strongly affected by the introduction of high content of PI. Therefore, an appropriate ratio between the two building blocks favors the formation of anisotropic microscale architecture. The synergistic effect between GO nanosheets and PI building blocks contributes to the elasticity of the nanocomposite, which is strongly affected by van der Waals attraction. Also, the thermal reduction of GO can enhance this cooperative effect, owing to the strong  $\pi$ – $\pi$  interaction of rGO.<sup>37</sup> Furthermore, PI building blocks act as a bridge between the neighboring giant graphene sheets, and some graphene flakes are even encapsulated by PI. This co-organized microstructure of the nanocomposite favors efficient load transfer between graphene nanosheets and PI building blocks, endowing the rGO/PI nanocomposite with excellent toughness and elasticity.

A schematic diagram concerning the contributions of conduction ( $\lambda_g$  for gas conduction and  $\lambda_{sol}$  for solid conduction), convection ( $\lambda_{conv}$ ) and radiation ( $\lambda_{rad}$ ) to the typical thermal transport mechanism of the rGO/PI nanocomposite is vividly illustrated in Fig. 4a. The synergistic effect between convection, conduction and radiation plays a critical part in determining the thermal conductivity of the anisotropic thermally insulating nanocomposite. The thermal insulation in different orientations of the nanocomposite, parallel and perpendicular to the freezing direction, was evaluated by the transient plane source (TPS) technique (Fig. S4†).<sup>44</sup> As shown in Fig. 4b, the thermal conductivity in the radial orientation is significantly lower than that in the axial direction for the rGO/PI nanocomposite with different contents of GO. In the case of the nanocomposite with the GO fraction of 10%, thermal conductivity normal to the tubular pores is  $0.022 \text{ W m}^{-1} \text{ K}^{-1}$  and that in axial orientation is slightly higher ( $0.027 \text{ W m}^{-1} \text{ K}^{-1}$ ). This is due to the randomly oriented three-dimensional (3D) framework, which is formed by the large volume shrinkage of the composite foam during the thermal treatment. The structural similarity in axial and radial directions contributes to no obvious difference in thermal insulation properties. Upon increasing the fraction of GO, the thermal conductivity of the rGO/PI nanocomposite in the axial direction exhibits a significant increase (from 0.027 to  $0.038 \text{ W m}^{-1} \text{ K}^{-1}$ ), whereas that in the radial direction apparently decreases (from 0.022 to  $0.012 \text{ W m}^{-1} \text{ K}^{-1}$ ). A high content of GO nanosheets can decrease the volume shrinkage and reduce the linkage of curled fibrils within



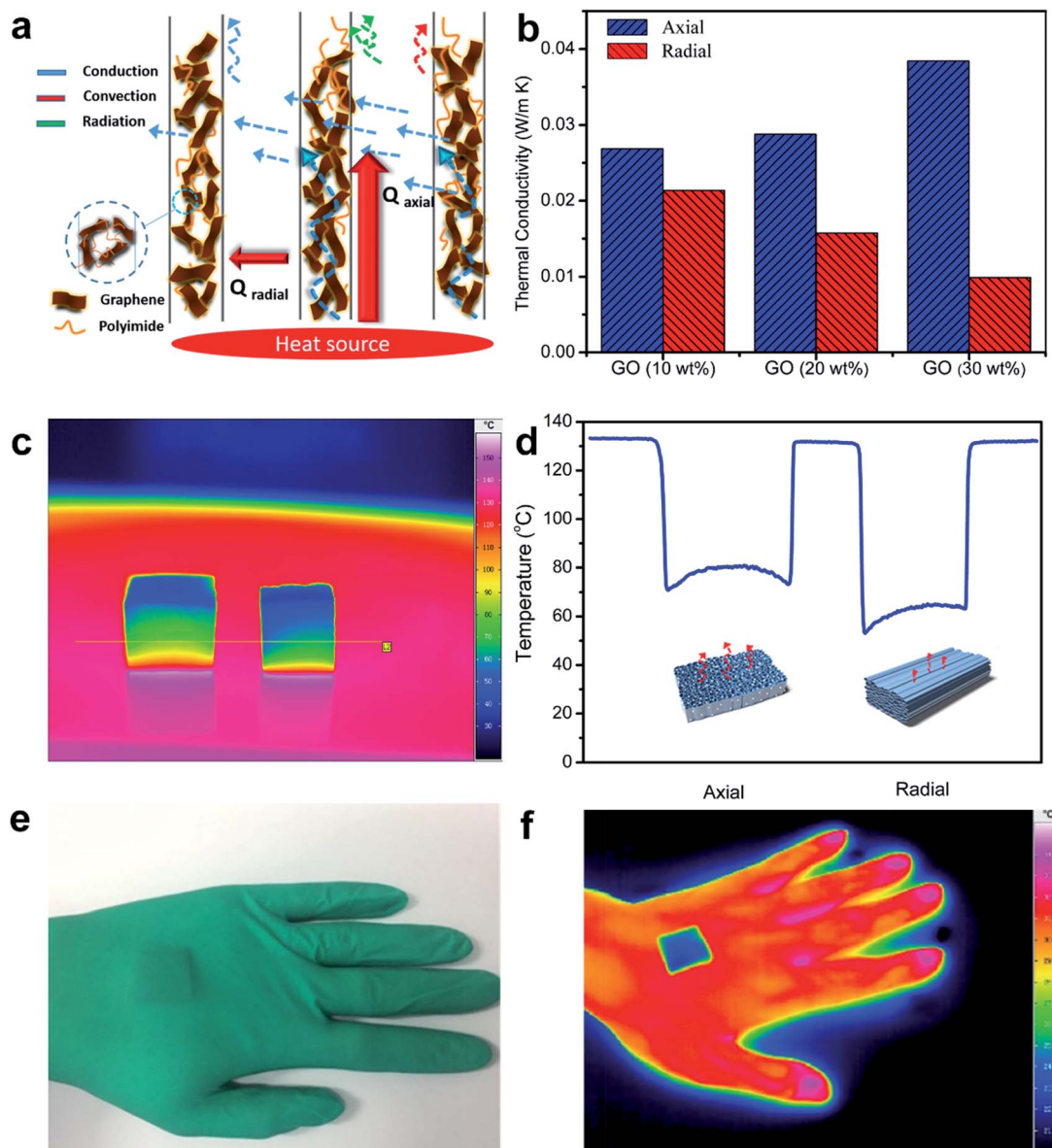


Fig. 4 Thermal insulation properties of the rGO/PI nanocomposite. (a) Thermal insulation mechanism analysis of the graphene–polyimide nanocomposite, (b) Thermal conductivity of the highly ordered rGO/PI nanocomposites with different GO contents. (c and d) Thermographic images of the highly ordered graphene–polyimide nanocomposite foam in the axial orientation and radial orientation and corresponding temperature distribution. (e and f) rGO/PI nanocomposite as a flexible and wearable thermal insulation filler in a glove.

the cell walls, leading to the reduction of thermal conductivity in the radial direction. Furthermore, an isotropic rGO/PI nanocomposite with identical composition and PI foam prepared with the same fabrication process was compared with the anisotropic rGO/PI nanocomposite to investigate the effect of anisotropic microstructures and composition ratio on the thermal conductivity (Fig. S5a and b†).

On the basis of these observations, we infer that the remarkable anisotropic thermal properties of the freeze-cast nanocomposite contribute to the synergistic effect of the highly ordered architecture and thermal properties of the nanosized components. The thermal transport in the radial direction can be significantly impeded by the anisotropic pore

and wall structure formed by the strong orientation effect (Fig. 4a). The interspacing within the nanostructured composite, which is smaller than the mean free path of air, can impede the thermal conduction through air.<sup>17</sup> Also, the thermal convection perpendicular to the aligned channels may be insignificant, for the reason that the size of tubular pores cannot meet the requirement for the onset of natural convection.<sup>45</sup> Moreover, the efficient infrared absorption property of carbonaceous materials can reduce the thermal radiation in insulating materials.<sup>46</sup> It is estimated that the nanosized pores in the cell walls can further reduce the thermal conductivity of the nanocomposite foam. This may be analogous to the effect of air pocket microstructures in rGO films and biomimetic porous





fibers.<sup>47–49</sup> However, the apparent thermal conductivities in the axial direction exhibit a tendency to increase, owing to the effective thermal conduction along the vertically aligned cell channels. The typical thermal transport mechanism of the rGO/PI nanocomposite can be ascribed to the highly ordered architecture formed by the strong orientation effect and the synergistic effect between orientation-dependent radiation, solid conduction of the nanostructured cell walls and insignificant natural convection along the cellular channels. The thermal properties of the nanosized components impart a typical interfacial thermal resistance (Kapitza resistance  $R_K$ ) and strong phonon scattering effects,<sup>18,50</sup> which play an important role in the reduction of solid conduction in the cell walls of the thermally insulating rGO/PI nanocomposite. Further analysis of the effect of the nanosized composition and microstructure on the thermal insulation properties can be found in the ESI (Table S1).†

The thermographic images of anisotropic heat transfer in both the axial and transverse directions of nanocomposite foam are visually illustrated in Fig. 4c and d. Temperature distribution in different directions of the rGO/PI nanocomposite shows anisotropic thermal insulation. As for the aligned cellular walls of the composite oriented perpendicular to the heat source plane, thermal energy can be conducted along the highly ordered channels, leading to a higher temperature distribution (about 76 °C). By comparison, the apparent lower temperature distribution (about 62 °C) reveals that the highly ordered microstructure endows the rGO/PI nanocomposite with efficient thermal insulation property in the radial orientation. We also put the nanocomposite as the filler in a glove to further evaluate the thermal insulation property (Fig. 4e, f). This phenomenon together with the good mechanical properties promises the application of the rGO/PI nanocomposite as a thermal insulation material.

## Conclusion

In summary, we have reported a thermally anisotropic rGO/PI nanocomposite prepared by the synergy of GO nanosheets and PI building blocks by the freeze-casting method. The newly developed rGO/PI nanocomposite (GO, 30 wt%) exhibits anisotropic thermal insulation properties with an ultralow thermal conductivity of  $0.012 \text{ W m}^{-1} \text{ K}^{-1}$  in the radial direction. The high performance of the thermally insulating nanocomposite is due to the synergistic effect of the highly ordered architecture and thermal properties of the nanosized components. The novel rGO/PI nanocomposite as a super-thermal insulation material could be beneficial for potential applications in personal wearable devices, thermal insulation materials for aerospace applications, and energy efficiency of buildings.

## Experimental section

### Materials

4,4'-Diaminodiphenyl ether (ODA, 98%), pyromellitic dianhydride (PMDA, 99%), *N,N*-dimethylacetamide (DMAc, 99%), triethylamine (TEA, 99%),  $\text{KMnO}_4$ ,  $\text{H}_2\text{SO}_4$  (98%),  $\text{H}_3\text{PO}_4$  (85%),

$\text{H}_2\text{O}_2$  (30%), and HCl (37%) were purchased from Sinopharm Chemical Reagent Co., Ltd. Natural graphite powder (325 mesh) was provided by Alfa-Aesar. All these reagents were used without further purification.

### Synthesis of graphene oxide

GO was synthesized based on the modified Hummers' method.<sup>51</sup> Expandable graphite powder (3 g) was mixed with a mixture of concentrated  $\text{H}_2\text{SO}_4/\text{H}_3\text{PO}_4$  (360/40 mL) and  $\text{KMnO}_4$  (18 g). After reaction at 50 °C for 10 h, the mixture was cooled to room temperature, poured into an ice bath (500 mL), and further treated with  $\text{H}_2\text{O}_2$  (30%, 5 mL). The bright-yellow suspension obtained was filtered, and the resulting solid material was washed successively with 10% HCl and deionized water by centrifugation (9500 rpm for 1 h). GO sheets were collected and then diluted to the desired concentration.

### Preparation of water-soluble polyimide precursor solution

Water-soluble PI precursor solution was synthesized according to the literature (Scheme S1†).<sup>28</sup> 4, 4'-ODA was dispersed in DMAc with a magnetic stirrer. Then, a quantity of PMDA was dissolved in the mixture with vigorous stirring for 5 h to obtain PAA solution. Note that the PMDA/4, 4'-ODA molar ratio was 100 : 99. The resultant solution was poured into excessive deionized water, and the produced precipitate was filtered, washed, and dried to remove the residual deionized water. After that, an ammonium salt solution of PAA ( $20 \text{ mg mL}^{-1}$ ) was prepared from PAA (1 g) and TEA (0.7 mL) in deionized water (49.3 mL) with stirring for 5 h at room temperature. Finally, the water-soluble polyimide precursor solution was obtained for further use.

### Preparation of the rGO/PI nanocomposite

The rGO/PI nanocomposite was fabricated in two steps, namely, freeze drying and thermal annealing. The ratio between GO and PI in the rGO/PI nanocomposite is determined by mass fraction. For the rGO/PI sample containing 10 wt% of GO, the mixed aqueous solution of GO ( $5 \text{ mg mL}^{-1}$ , 10 mL) and water-soluble polyimide precursor ( $20 \text{ mg mL}^{-1}$ , 22.5 mL) were stirred for 0.5 h. Then, the suspensions were subjected to freeze-casting by controlled freezing in a liquid-nitrogen bath. The obtained sample was subjected to freeze drying for 36 h followed by thermal annealing at 300 °C in an argon atmosphere for 2 h. Monolithic rGO/PI nanocomposites with different contents of GO were obtained by the same procedure.

## Conflicts of interest

There are no conflicts to declare.

## References

- 1 J. L. Reyna and M. V. Chester, Energy efficiency to reduce residential electricity and natural gas use under climate change, *Nat. Commun.*, 2017, **8**, 14916.



- 2 U.S. Department of Energy, *Guiding Principles for Sustainable Federal Buildings*, 2016, <https://energy.gov/eere/femp/guiding-principles-sustainable-federal-buildings>.
- 3 P.-C. Hsu, A. Y. Song, P. B. Catrysse, C. Liu, Y. Peng, J. Xie, S. Fan and Y. Cui, Radiative human body cooling by nanoporous polyethylene textile, *Science*, 2016, **353**, 1019–1023.
- 4 Y. Guo, K. Li, C. Hou, Y. Li, Q. Zhang and H. Wang, Fluoroalkylsilane-Modified Textile-Based Personal Energy Management Device for Multifunctional Wearable Applications, *ACS Appl. Mater. Interfaces*, 2016, **8**, 4676–4683.
- 5 M. LaFrance, *Technology Roadmap: Energy Efficient Building Envelopes*, IEA. Paris, 2013.
- 6 B. P. Jelle, Traditional, state-of-the-art and future thermal building insulation materials and solutions – Properties, requirements and possibilities, *Energy Build.*, 2011, **43**, 2549–2563.
- 7 M. S. Al-Homoud, Performance characteristics and practical applications of common building thermal insulation materials, *Build. Environ.*, 2005, **40**, 353–366.
- 8 H. S. Kim, T. Wang, W. Liu and Z. Ren, Engineering thermal conductivity for balancing between reliability and performance of bulk thermoelectric generators, *Adv. Funct. Mater.*, 2016, **26**, 3678–3686.
- 9 J. P. Heremans, M. S. Dresselhaus, L. E. Bell and D. T. Morelli, When thermoelectrics reached the nanoscale, *Nat. Nanotechnol.*, 2013, **8**, 471–473.
- 10 Y. Hu, L. Zeng, A. J. Minnich, M. S. Dresselhaus and G. Chen, Spectral mapping of thermal conductivity through nanoscale ballistic transport, *Nat. Nanotechnol.*, 2015, **10**, 701–706.
- 11 N. Leventis, C. Chidambareswarapattar, D. P. Mohite, Z. J. Larimore, H. Lu and C. Sotiriou-Leventis, Multifunctional porous aramids (aerogels) by efficient reaction of carboxylic acids and isocyanates, *J. Mater. Chem.*, 2011, **21**, 11981–11986.
- 12 A. Rigacci, J. C. Marechal, M. Repoux, M. Moreno and P. Achard, Preparation of polyurethane-based aerogels and xerogels for thermal superinsulation, *J. Non-Cryst. Solids*, 2004, **350**, 372–378.
- 13 M. D. Gawryla, M. Nezamzadeh and D. A. Schiraldi, Foam-like materials produced from abundant natural resources, *Green Chem.*, 2008, **10**, 1078–1081.
- 14 A. M. Papadopoulos, State of the art in thermal insulation materials and aims for future developments, *Energy Build.*, 2005, **37**, 77–86.
- 15 D. Bozsaky, The historical development of thermal insulation materials, *Periodica Polytechnica Architecture*, 2010, **41**, 49–56.
- 16 N. Hüsing and U. Schubert, Aerogels—Airy Materials: Chemistry, Structure, and Properties, *Angew. Chem., Int. Ed.*, 1998, **37**, 22–45.
- 17 T. Li, J. Song, X. Zhao, Z. Yang, G. Pastel, S. Xu, C. Jia, J. Dai, C. Chen, A. Gong, F. Jiang, Y. Yao, T. Fan, B. Yang, L. Wågberg, R. Yang and L. Hu, Anisotropic, lightweight, strong, and super thermally insulating nanowood with naturally aligned nanocellulose, *Sci. Adv.*, 2018, **4**, eaar3724.
- 18 B. Wicklein, A. Kocjan, G. Salazar-Alvarez, F. Carosio, G. Camino, M. Antonietti and L. Bergström, Thermally insulating and fire-retardant lightweight anisotropic foams based on nanocellulose and graphene oxide, *Nat. Nanotechnol.*, 2014, **10**, 277.
- 19 T. Borca-Tasciuc, S. Vafaei, D.-A. Borca-Tasciuc, B. Q. Wei, R. Vajtai and P. M. Ajayan, Anisotropic thermal diffusivity of aligned multiwall carbon nanotube arrays, *J. Appl. Phys.*, 2005, **98**, 054309.
- 20 C. Wan, X. Gu, F. Dang, T. Itoh, Y. Wang, H. Sasaki, M. Kondo, K. Koga, K. Yabuki, G. J. Snyder, R. Yang and K. Koumoto, Flexible n-type thermoelectric materials by organic intercalation of layered transition metal dichalcogenide  $\text{TiS}_2$ , *Nat. Mater.*, 2015, **14**, 622–627.
- 21 J. Liu, B. Yoon, E. Kuhlmann, M. Tian, J. Zhu, S. M. George, Y.-C. Lee and R. Yang, Ultralow thermal conductivity of atomic/molecular layer-deposited hybrid organic–inorganic zinc oxide thin films, *Nano Lett.*, 2013, **13**, 5594–5599.
- 22 C. Chiritescu, D. G. Cahill, N. Nguyen, D. Johnson, A. Bodapati, P. Keblinski and P. Zschack, Ultralow thermal conductivity in disordered, layered  $\text{WSe}_2$  crystals, *Science*, 2007, **315**, 351–353.
- 23 M. D. Losego, I. P. Blitz, R. A. Vaia, D. G. Cahill and P. V. Braun, Ultralow thermal conductivity in organoclay nanolaminates synthesized *via* simple self-assembly, *Nano Lett.*, 2013, **13**, 2215–2219.
- 24 J. Wan, J. Song, Z. Yang, D. Kirsch, C. Jia, R. Xu, J. Dai, M. Zhu, L. Xu, C. Chen, Y. Wang, Y. Wang, E. Hitz, S. D. Lacey, Y. Li, B. Yang and L. Hu, *Adv. Mater.*, 2017, **29**, 1703331.
- 25 J.-K. Yu, S. Mitrovic, D. Tham, J. Varghese and J. R. Heath, Reduction of thermal conductivity in phononic nanomesh structures, *Nat. Nanotechnol.*, 2010, **5**, 718.
- 26 M. D. Losego, M. E. Grady, N. R. Sottos, D. G. Cahill and P. V. Braun, Effects of chemical bonding on heat transport across interfaces, *Nat. Mater.*, 2012, **11**, 502.
- 27 X. Lu, M. C. Arduini-Schuster, J. Kuhn, O. Nilsson, J. Fricke and R. W. Pekala, Thermal Conductivity of Monolithic Organic Aerogels, *Science*, 1992, **255**, 971–972.
- 28 Y. Qin, Q. Peng, Y. Ding, Z. Lin, C. Wang, Y. Li, F. Xu, J. Li, Y. Yuan, X. He and Y. Li, Lightweight, Superelastic, and Mechanically Flexible Graphene/Polyimide Nanocomposite Foam for Strain Sensor Application, *ACS Nano*, 2015, **9**, 8933–8941.
- 29 J. Feng, X. Wang, Y. Jiang, D. Du and J. Feng, Study on Thermal Conductivities of Aromatic Polyimide Aerogels, *ACS Appl. Mater. Interfaces*, 2016, **8**, 12992–12996.
- 30 H. Guo, M. A. B. Meador, L. McCorkle, D. J. Quade, J. Guo, B. Hamilton, M. Cakmak and G. Sprowl, Polyimide Aerogels Cross-Linked through Amine Functionalized Polyoligomeric Silsesquioxane, *ACS Appl. Mater. Interfaces*, 2011, **3**, 546–552.
- 31 S. Deville, E. Saiz, R. K. Nalla and A. P. Tomsia, Freezing as a Path to Build Complex Composites, *Science*, 2006, **311**, 515–518.
- 32 C. Wang, X. Chen, B. Wang, M. Huang, B. Wang, Y. Jiang and R. S. Ruoff, Freeze-Casting Produces a Graphene Oxide





- Aerogel with a Radial and Centrosymmetric Structure, *ACS Nano*, 2018, **12**, 5816–5825.
- 33 Q. Peng, Y. Qin, X. Zhao, X. Sun, Q. Chen, F. Xu, Z. Lin, Y. Yuan, Y. Li, J. Li, W. Yin, C. Gao, F. Zhang, X. He and Y. Li, Superlight, Mechanically Flexible, Thermally Superinsulating, and Antifrosting Anisotropic Nanocomposite Foam Based on Hierarchical Graphene Oxide Assembly, *ACS Appl. Mater. Interfaces*, 2017, **9**, 44010–44017.
- 34 L. Qiu, J. Z. Liu, S. L. Y. Chang, Y. Wu and D. Li, Biomimetic superelastic graphene-based cellular monoliths, *Nat. Commun.*, 2012, **3**, 1241.
- 35 O.-K. Park, M. G. Hahm, S. Lee, H.-I. Joh, S.-I. Na, R. Vajtai, J. H. Lee, B.-C. Ku and P. M. Ajayan, *In situ* Synthesis of Thermochemically Reduced Graphene Oxide Conducting Nanocomposites, *Nano Lett.*, 2012, **12**, 1789–1793.
- 36 Z. Zeng, Y. Zhang, X. Y. D. Ma, S. I. S. Shahabadi, B. Che, P. Wang and X. Lu, Biomass-based honeycomb-like architectures for preparation of robust carbon foams with high electromagnetic interference shielding performance, *Carbon*, 2018, **140**, 227–236.
- 37 H. Sun, Z. Xu and C. Gao, Multifunctional, Ultra-Flyweight, Synergistically Assembled Carbon Aerogels, *Adv. Mater.*, 2013, **25**, 2554–2560.
- 38 Z. Xu, B. Zheng, J. Chen and C. Gao, Highly Efficient Synthesis of Neat Graphene Nanoscrolls from Graphene Oxide by Well-Controlled Lyophilization, *Chem. Mater.*, 2014, **26**, 6811–6818.
- 39 T. Ramanathan, A. A. Abdala, S. Stankovich, D. A. Dikin, M. Herrera-Alonso, R. D. Piner, D. H. Adamson, H. C. Schniepp, X. Chen, R. S. Ruoff, S. T. Nguyen, I. A. Aksay, R. K. Prud'Homme and L. C. Brinson, Functionalized graphene sheets for polymer nanocomposites, *Nat. Nanotechnol.*, 2008, **3**, 327–331.
- 40 J.-Y. Hong, B. M. Bak, J. J. Wie, J. Kong and H. S. Park, Reversibly Compressible, Highly Elastic, and Durable Graphene Aerogels for Energy Storage Devices under Limiting Conditions, *Adv. Funct. Mater.*, 2015, **25**, 1053–1062.
- 41 C. Wu, X. Huang, X. Wu, R. Qian and P. Jiang, Mechanically Flexible and Multifunctional Polymer-Based Graphene Foams for Elastic Conductors and Oil–Water Separators, *Adv. Mater.*, 2013, **25**, 5658–5662.
- 42 A. Cao, P. L. Dickrell, W. G. Sawyer, M. N. Ghasemi-Nejhad and P. M. Ajayan, Super-Compressible Foamlike Carbon Nanotube Films, *Science*, 2005, **310**, 1307–1310.
- 43 R. Zhang, Q. Chen, Z. Zhen, X. Jiang, M. Zhong and H. Zhu, Cellulose-Templated Graphene Monoliths with Anisotropic Mechanical, Thermal, and Electrical Properties, *ACS Appl. Mater. Interfaces*, 2015, **7**, 19145–19152.
- 44 S. E. Gustafsson, E. Karawacki and M. N. Khan, Determination of the thermal-conductivity tensor and the heat capacity of insulating solids with the transient hotstrip method, *J. Appl. Phys.*, 1981, **52**, 2596.
- 45 L. Glicksman, N. Hilyard and A. Cunningham, *Low Density Cellular Plastics: Physical Basis of Behaviour*, Chapman and Hall, London 1994.
- 46 A. A. Balandin, Thermal properties of graphene and nanostructured carbon materials, *Nat. Mater.*, 2011, **10**, 569.
- 47 J. D. Renteria, S. Ramirez, H. Malekpour, B. Alonso, A. Centeno, A. Zurutuza, A. I. Cocemasov, D. L. Nika and A. A. Balandin, Strongly Anisotropic Thermal Conductivity of Free-Standing Reduced Graphene Oxide Films Annealed at High Temperature, *Adv. Funct. Mater.*, 2015, **25**, 4664–4672.
- 48 H.-J. Zhan, K.-J. Wu, Y.-L. Hu, J.-W. Liu, H. Li, X. Guo, J. Xu, Y. Yang, Z.-L. Yu, H.-L. Gao, X.-S. Luo, J.-F. Chen, Y. Ni and S.-H. Yu, *Chem*, 2019, **5**, 1871–1882.
- 49 Y. Cui, H. Gong, Y. Wang, D. Li and H. Bai, *Adv. Mater.*, 2018, **30**, 1706807.
- 50 C. Hu, M. Kiene and P. S. Ho, Thermal conductivity and interfacial thermal resistance of polymeric low k films, *Appl. Phys. Lett.*, 2001, **79**(25), 4121–4123.
- 51 D. C. Marcano, D. V. Kosynkin, J. M. Berlin, A. Sinitskii, Z. Sun, A. Slesarev, L. B. Alemany, W. Lu and J. M. Tour, Improved Synthesis of Graphene Oxide, *ACS Nano*, 2010, **4**, 4806–4814.

